SCIENTIFIC REPORTS

natureresearch

OPEN

Role of precursors mixing sequence on the properties of CoMn$_2$O$_4$ cathode materials and their application in pseudocapacitor

Bhaskar Pattanayak[1,2], Firman Mangasa Simanjuntak[3], Debashis Panda[2,4], Chih - Chieh Yang[2], Amit Kumar[5], Phuoc – Anh Le[5], Kung – Hwa Wei[5] & Tseung –Yuen Tseng[1,2]*

In this study, the effect of oxygen vacancy in the CoMn$_2$O$_4$ on pseudocapacitive characteristics was examined, and two tetragonal CoMn$_2$O$_4$ spinel compounds with different oxygen vacancy concentrations and morphologies were synthesized by controlling the mixing sequence of the Co and Mn precursors. The mixing sequence was changed; thus, morphologies were changed from spherical nanoparticles to nanoflakes and oxygen vacancies were increased. Electrochemical studies have revealed that tetragonal CoMn$_2$O$_4$ spinels with a higher number of oxygen vacancies exhibit a higher specific capacitance of 1709 F g^{-1} than those with a lower number of oxygen vacancies, which have a higher specific capacitance of 990 F g^{-1}. Oxygen vacancies create an active site for oxygen ion intercalation. Therefore, oxidation–reduction reactions occur because of the diffusion of oxygen ions at octahedral/tetrahedral crystal edges. The solid-state asymmetric pseudocapacitor exhibits a maximum energy density of 32 Wh-kg^{-1} and an excellent cyclic stability of nearly 100%.

Energy storage components have received considerable attention in the design of small microelectronic devices. Pseudocapacitors are essential devices for energy storage applications because of their high power densities, rapid charge–discharge rate, and long lifecycle[1]. For renewable and sustainable energy applications, the adoption of new nanostructured materials is crucial for manufacturing hybrid supercapacitors[2]. Metal oxides with a spinel crystal structure of AB$_2$X$_4$, where A and B are metal and X is oxygen, are preferred materials for manufacturing hybrid supercapacitors because of their larger specific capacitances and superior energy storage ability compared with carbon-based supercapacitors[3,4]. Among various types of spinel structures, cobalt manganese oxide (i.e., Co$_{3-x}$Mn$_x$O$_4$) has distinct characteristics and excellent advantages in the field of charge storage devices. The presence of multiple valences of cations (Co and Mn ions) demonstrates excellent electrochemical behaviour. However, the effect of oxygen vacancy defects in Co$_{3-x}$Mn$_x$O$_4$-based pseudocapacitor devices has not yet been investigated.

Various synthesised methods have been proposed for producing spinel-structured materials, such as solid-state reactions[3,5], the sol–gel[6] method, the hydrothermal method[7], and the co-precipitation method[8]. However, most methods require high temperatures and considerable amounts of time, which hinder their applications. Because high-temperature processing engenders irregular structures, with a low surface area and large particle size, it is associated with unsatisfactory chemical properties[7–9].

In this study, an air oxidation precipitation method was adopted to synthesise the tetragonal CoMn$_2$O$_4$ spinel oxides, where the crystalline spinel was fabricated at a lower temperature and in less time than those in other studies. High-temperature annealing in air and argon atmospheres have been reported to successfully generate oxygen vacancies[10,11]. Furthermore, the solvothermal method can generate oxygen vacancies but requires a long period of time[12]. This method allowed us to modulate the oxygen vacancy concentration in CoMn$_2$O$_4$ by merely varying the precursor mixing sequence without changing precursor ingredients. Therefore, structural and morphological studies were conducted using X-ray diffraction (XRD), scanning electron microscopy (SEM), and

[1]Department of Electrical Engineering and Computer Science, National Chiao Tung University, Hsinchu, 30010, Taiwan. [2]Institute of Electronics, National Chiao Tung University, Hsinchu, 30010, Taiwan. [3]WPI-Advanced Institute for Materials Research, Tohoku University, Sendai, 980-8577, Japan. [4]Department of Physics, National Institute of Science and Technology, Berhampur, Orissa, 761008, India. [5]Department of Materials Science and Engineering, National Chiao Tung University, Hsinchu, 30010, Taiwan. *email: tseng@cc.nctu.edu.tw
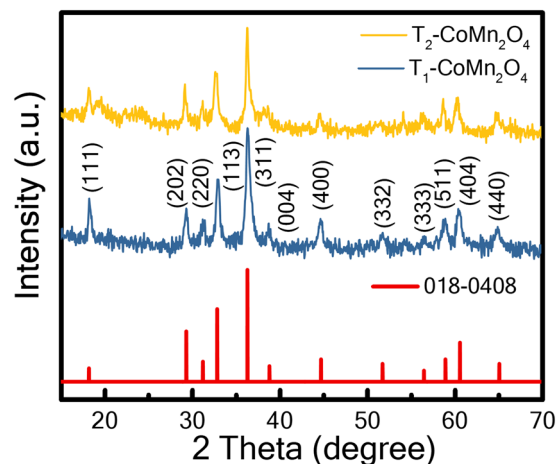
Figure 1. (a) X-ray diffraction spectra of synthesised T_1-CoMn$_2$O$_4$ and T_2-CoMn$_2$O$_4$. Experimental data with Bragg diffraction position are marked by a blue line (T_1-CoMn$_2$O$_4$), a yellow line (T_2-CoMn$_2$O$_4$), and red bars.

transmission electron microscopy (TEM) analyses. The effect of oxygen vacancies on the energy storage behaviour of cathode materials was investigated using X-ray photoelectron spectroscopy (XPS).

Results and Discussion

Figure 1 shows the XRD spectra of T_1 and T_2 samples. The obtained Bragg's diffraction patterns were matched with the standard JCPDS data file (no #18-0408), which validated the formation of the tetragonal structure of CoMn$_2$O$_4$ with a mixed spinel (Co, Mn) (Co, Mn)$_2$O$_4$[11]. The strong peaks in the spectra indicated that the as-synthesised T_1 and T_2 had satisfactory crystallinity.

Figure 2 shows the SEM and TEM micrographs of T_1 and T_2. Figure 2(a,b) show SEM images of T_1 and T_2, respectively, which indicate that T_1 comprises uniformly distributed spherical nanoparticles, whereas T_2 primarily comprises nanoflakes and a few nanoparticles with a square structure. Figure 2(c,d) illustrate TEM images of T_1 and T_2, respectively, and T_1 and T_2 nanoparticles are aggregated with an average particle size of approximately 23 and 27 nm, respectively [insets of Fig. 2(c,d)]. Moreover, similar nanoparticle sizes were reported in spinel CoMn$_2$O$_4$ nanoparticles supported on nitrogen phosphorus-doped graphene electrode materials by He's group, in which the range of particle sizes was 5–25 nm[13]. Therefore, T_2 has higher conductivity than T_1, which is validated by electrochemical impedance spectroscopy (EIS). To identify the phase of the samples, high-resolution transmission electron microscopy was performed on T_1 and T_2 nanostructures [as shown in Fig. 2(e–g)], respectively. The selected area electron diffraction (SAED) patterns of T_1 and T_2 reveal crystal diffraction with planes of (220), (311), (440), (111), (404), (332), and (511) for T_1 and T_2 [insets of Fig. 2(e–g)], which validate the formation of the tetragonal spinel crystal structure. The lattice fringes of T_1 nanoparticles show (311) plane orientation with interplanar spacing of 2.5 Å, and those of T_2 samples show (111) plane orientation with interplanar spacing of 4.8 Å [insets of Fig. 2(e,f)]. However, nanoflakes exhibit lattice fringes of (400), (311), and (111) for T_2 [Fig. 2(g)]. This result was consistent with XRD results (Fig. 1).

The surface area and porosity of the electrodes are crucial in the performance of pseudocapacitor devices[14,15]; therefore, a Brunauer–Emmett–Teller (BET) surface area measurement was performed. Figure 3 shows nitrogen adsorption–desorption isotherms at 77 K of T_1 and T_2. According to the definite hysteresis loop of IUPAC classification, the isotherms of both spinels are classified as type IV, which corresponds to the mesoporous structure[13,16,17]. The availability of hysteresis loop intermediate $P/P_0 = 0.5$ to 1 confirms the mesoporous nature of both compounds[15]. A high adsorption P/P_0 at 0.9 to 1 indicates the performance of the macroporous part to the overall surface area of T_1 and T_2[14]. The BET surface areas and the corresponding pore volumes of T_1 and T_2 are 53.21 m²/g (0.32 cm³/g) and 44.47 m²/g (0.23 cm³/g), respectively. A higher surface area corresponds to a smaller grain size[18]. The pore-size distribution curve can be obtained through N$_2$ adsorption–desorption isotherms by using the Barrett–Joyner–Halenda (BJH) method (inset of Fig. 3). The average pore sizes of T_1 and T_2 are 20.0 and 20.8 nm, respectively.

An XPS analysis was conducted to evaluate defects and oxidation states in the CoMn$_2$O$_4$ spinel structure. Figure 4 shows the XPS spectra of Co2p, Mn2p, Mn3s, and O1s core levels of pure T_1 and T_2 samples. Figure 4(a) presents the Co2p spectra of T_1 and T_2, respectively, indicating that there are doublet peaks of Co 2p$_{3/2}$ and Co 2p$_{1/2}$ located at 780.46 and 795.96 eV for T_1 and 780.62 and 796 eV for T_2, respectively. The energy splitting (ΔE) values of the divalent and trivalent Co ions are 15.4 and 15.1 eV for T_1 and T_2, respectively, which are consistent with values reported in the literature[19]. The Co2p spectra of T_1 and T_2 are fitted into six peaks with binding energies of approximately 780.4 and 795.8 eV for Co^{2+} and 782.2 and 797.3 eV for Co^{3+}[5,19]. Furthermore, two satellite peaks are observed at 786.13 and 802.6 eV for T_1 and 785.84 and 802.45 eV for T_2, respectively[19]. The concentrations of Co^{2+} and Co^{3+} are 63% and 37% for T_1 and 70% and 30% for T_2, respectively(as listed in Table 1).

Figure 4(b,c) show the Mn 2p and Mn 3 s spectra of T_1 and T_2, respectively. Figure 4(b) shows the Mn 2p spectra combined with 2p$_{3/2}$ and 2p$_{1/2}$ located at approximately 641.9 and 653.8 eV for T_1 and 642 and 653.7 eV for T_2, respectively. The Mn2p$_{3/2}$ and Mn2p$_{1/2}$ of T_1 are deconvoluted into sub-peaks located at approximately 641.39
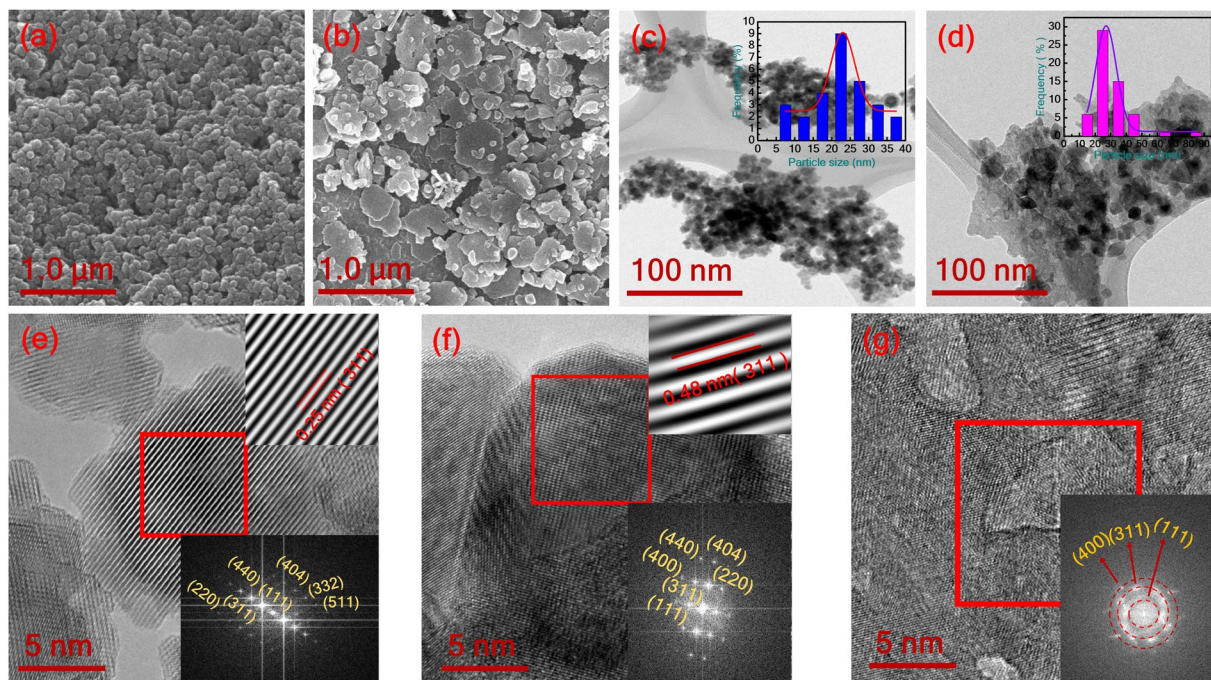
Figure 2. (**a,b**) Scanning electron microscopy images of T_1-CoMn$_2$O$_4$ and T_2-CoMn$_2$O$_4$ and (**c,d**) transmission electron microscopy images of T_1-CoMn$_2$O$_4$ and T_2-CoMn$_2$O$_4$ with particle size distribution (inset). High-resolution transmission electron microscopy images and the corresponding fast Fourier transform of (**e**) T_1-CoMn$_2$O$_4$ and (**f,g**) T_2-CoMn$_2$O$_4$.
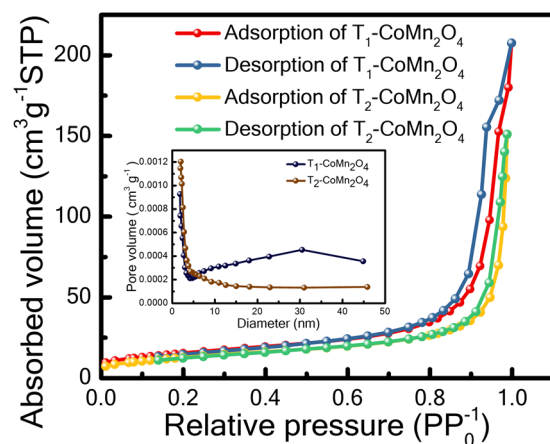

Figure 3. Brunauer–Emmett–Teller surface area of T_1-CoMn$_2$O$_4$ and T_1-CoMn$_2$O$_4$; inset presents pore-size distribution.

and 652.91 eV for Mn^{3+} and 642.5 and 654 for Mn^{2+} states, respectively. Furthermore, those of the T_2 sample are deconvoluted into sub-peaks located at approximately 641.2 and 652.91 eV corresponding to Mn^{3+} and 642.5 and 653.9 eV for Mn^{2+} states[20]. The concentrations of Mn^{2+} and Mn^{3+} in T_1 are 73% and 27%, respectively, whereas those for T_2 are 82% and 18%, respectively (Table 1). To ensure peak splitting and doublet, the parallel spin coupling of Mn 3 s of T_1 and T_2 were analysed, and Fig. 4(c) depicts the results. Mn 3 s core level spectra show binding energies at approximately 83.9 and 89.3 eV for T_1 and 83.9 and 89.5 eV for T_2. The energy separation for T_1 is 5.4 eV, which is lower than that for T_2, (5.6 eV) [Fig. 4(c)], indicating the dominance of lower Mn valance[10,21–23]. Figure 4(d) shows the peak fitting for the O1s core level of both T_1 and T_2 indicating that three peaks are observed at approximately 530.16 (O$_i$), 531.67 (O$_{ii}$), and 533 eV (O$_{iii}$) for T_1 and 530.2 (O$_i$), 531.49 (O$_{ii}$), and 533.14 eV (O$_{iii}$) for T_2. The O$_i$, O$_{ii}$, and O$_{iii}$ correspond to lattice oxygen bonding with metal (Co, Mn) O$_{metal-oxygen}$, non-lattice oxygen (oxygen vacancies), and oxygen absorbed on the surface in the form of OH$^-$, respectively. Figure 4(d) presents that the large area covered by the O$_{ii}$ peak indicates the presence of higher oxygen vacancies in T_2[11,24]. The percentages of oxygen vacancies in T_1 and T_2 samples are 35% and 72%, respectively.
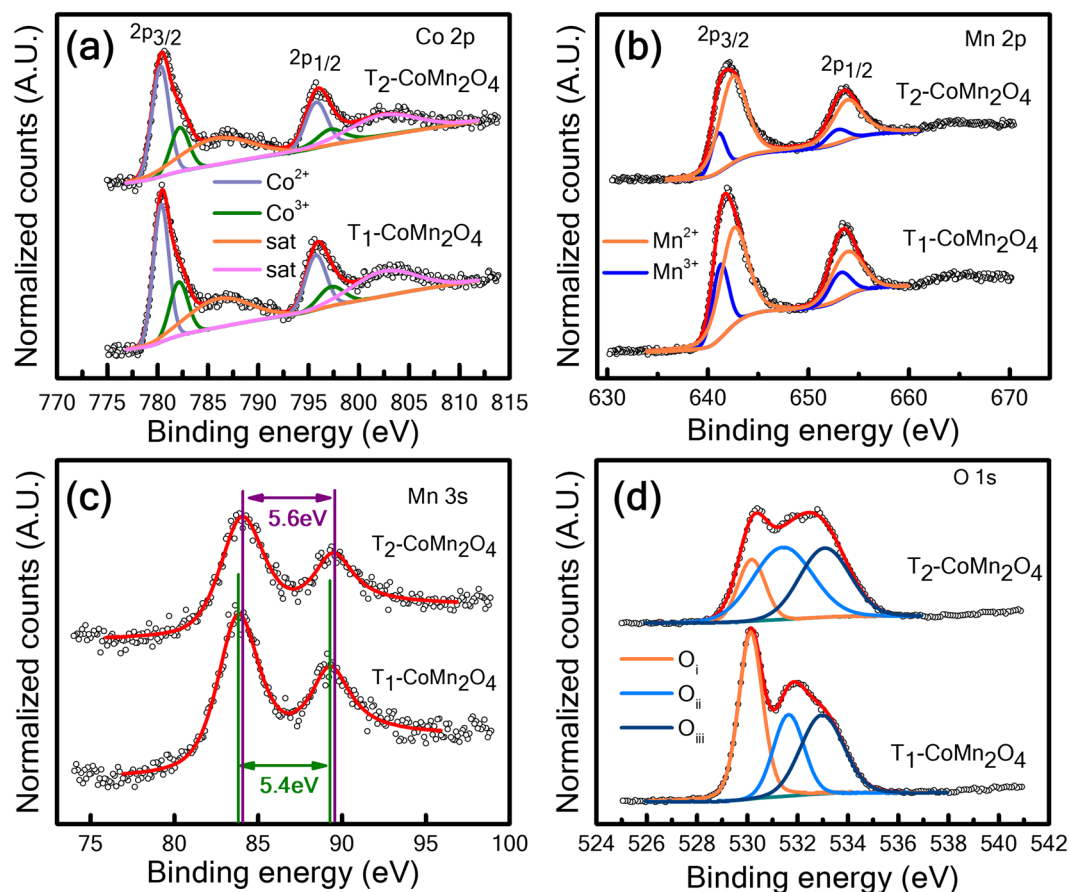
Figure 4. X-ray photoelectron spectra of the synthesised spinel (**a**) Co 2p of T_1-$CoMn_2O_4$ and T_2-$CoMn_2O_4$, respectively; (**b,c**) Mn 2p and Mn 3 s of T_1-$CoMn_2O_4$ and T_2-$CoMn_2O_4$, respectively; (**d**) O 1 s spectra of T_1-$CoMn_2O_4$ and T_2-$CoMn_2O_4$, respectively.

Valance states	T_1-$CoMn_2O_4$ (%)	T_2-$CoMn_2O_4$ (%)
Co^{3+}	37	30
Co^{2+}	63	70
Mn^{2+}	73	82
Mn^{3+}	27	18

Table 1. Various valence numbers of ions in T_1 and T_2 from X-ray photoelectron spectroscopy data. Pattanayak *et al.*, Table 1.

Electrochemical performance examinations of T_1 and T_2 electrodes were conducted using a three-electrode cell system. The cyclic voltammetry (CV) responses of T_1, T_2, and bare Ni foam are presented in Fig. 5(a) at a scan rate of $20\,mV\,s^{-1}$ in a voltage window from -0.1 to $0.6\,V$ and indicate that both T_1 and T_2 exhibit oxidation and reduction redox peaks at approximately 0.2 and 0.5 V, respectively, because of the Faradic reaction. The quasi-reversible Faradic reaction with redox peaks for T_1 and T_2 reveals the occurrence of surface redox reactions, which are provided as follows[25,26].
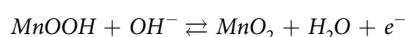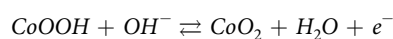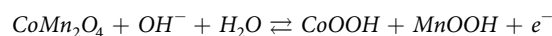
$$CoMn_2O_4 + OH^- + H_2O \rightleftarrows CoOOH + MnOOH + e^-$$

$$CoOOH + OH^- \rightleftarrows CoO_2 + H_2O + e^-$$

$$MnOOH + OH^- \rightleftarrows MnO_2 + H_2O + e^-$$

Figure 5(b,c) show the CV responses of T_1 and T_2 at a scan rate from 5 to $200\,mV\,s^{-1}$ at -0.1 to $0.6\,V$, respectively. Moreover, no significant changes are observed in the shape of CV curves when the scan rate increased from 5 to $200\,mV\,s^{-1}$, indicating that both electrodes have satisfactory electronic conduction and low equivalent series resistance[27]. Because of the kinetics of redox reactions, the current increases with the increasing scan rate
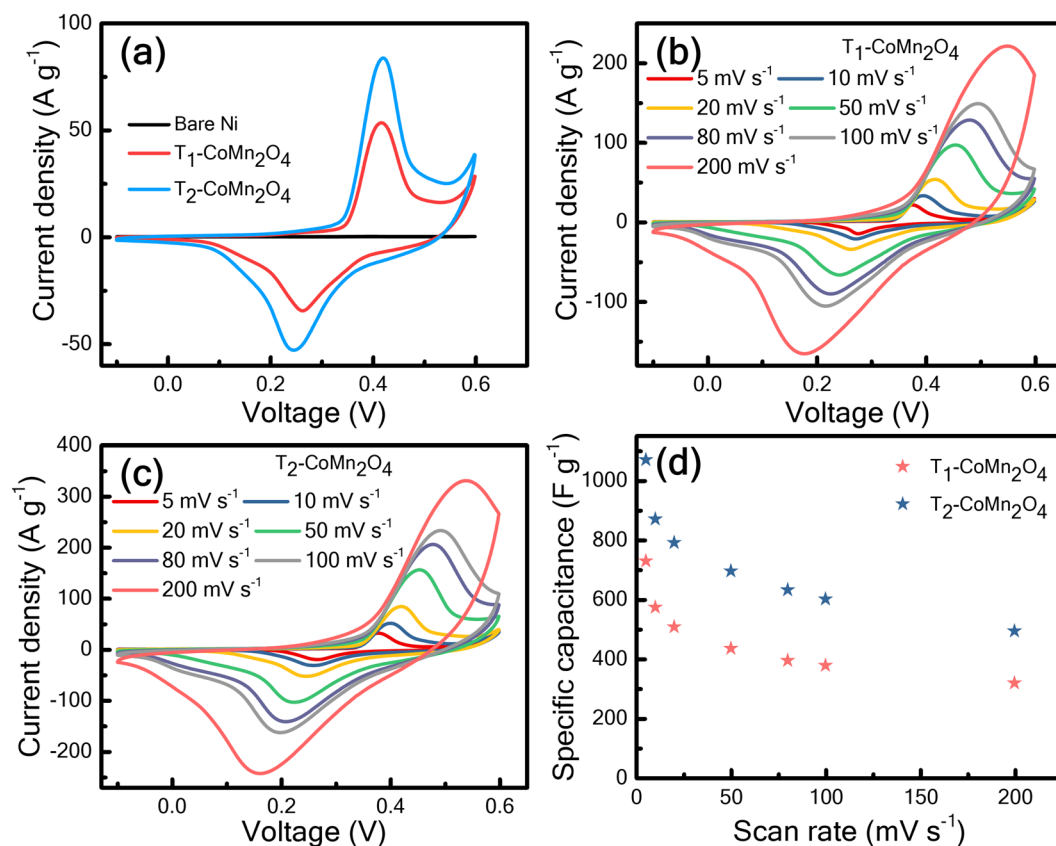
Figure 5. Electrochemical characterisation of spinel material electrodes: (**a**) the cyclic voltammetry responses of bare Ni foam T_1-CoMn$_2$O$_4$ and T_2-CoMn$_2$O$_4$, respectively, at 5 mV s^{-1}; (**b,c**) cyclic voltammetry responses of T_1-CoMn$_2$O$_4$ and T_2-CoMn$_2$O$_4$, respectively, at a scan rate of 5–200 mV s^{-1}; (**d**) variation in the specific capacitance with the scan rate for two electrodes.

in accordance with Ohm's law[26]. Because of the internal resistance between the electrode and electrolyte ions, the anodic peaks show red shift of 0.17 V and cathodic peaks blue shift of 0.1 V with the increasing scan rate for T_1 which is higher than T_2 (0.16 V for the anodic scan and 0.1 V for the cathodic scan) [Fig. 5(b,c)][27,28]. The reduced peak shifting of T_2 indicates that a lower overpotential is required for ionic transport because of a high current response at higher scan rates. Therefore, T_2 shows a higher rate capability than T_1.

Specific capacitance (F g^{-1}) can be estimated from the CV curve by using the following equation[14,18]:

$$C_{sp} = \frac{\int_{V_1}^{V_2} I(V)dV}{m\gamma(V_2 - V_1)} \tag{1}$$

where γ, m, ($V_2 - V_1$), and I represent the scan rate, mass of active materials, voltage window, and current response, respectively. Figure 5(b,c) show that the specific capacitances (C_{sp}) of T_1 and T_2 calculated using Eq. (1) are 730 and 1071 F g^{-1} at 5 mV s^{-1}, respectively. The scan rate dependence C_{sp} [Fig. 5(d)] indicates that C_{sp} values of T_1 and T_2 decrease with the increasing scan rate, which is attributed to the decreasing redox active sites with an electrolyte at high scan rates[14,29]. The mesoporous structure in the electrodes creates low-resistance pathways for ion diffusion and increased charge transport. Therefore, electrolyte ions are soaked by the mesoporous wall and increase the capacity of the electroactive channel for high charge storage at a high scan rate[16]. The area under the CV curve of T_2 is larger than that of T_1, thereby improving capacitive performance and ionic conductivity. Because both T_1 and T_2 electrodes are constructed using nanocrystalline materials with a mesoporous structure, electrolyte ions could be transported through their nanochannels[14]. When the scan rate increased to 200 mV s^{-1}, T_1 and T_2 show specific capacitance of 318 and 493 F g^{-1} with 43% and 46% retention of the initial capacitances, respectively. The variation in charge storage efficiency may be attributed to the difference between the crystallite size and surface morphology of T_1 and T_2.

CV performance was significant for the inflction of potential in pseudocapacitive devices. Furthermore, charge–discharge behaviour was one of the most crucial characteristics. Figure 6(a) exhibits that the charge–discharge characteristics of T_1 and T_2 are −0.2 to 0.5 V at a current density of 1 A g^{-1}, indicating that the discharge profile is nonlinear, which is prominent pseudocapacitance within this potential window. These discharge profiles can be divided into two parts. One part varies nonlinearly from 0.5 to approximately 0.25 V, suggesting pseudocapacitor behaviour, whereas the other parameter varies from approximately 0.25 to −0.2 V, indicating
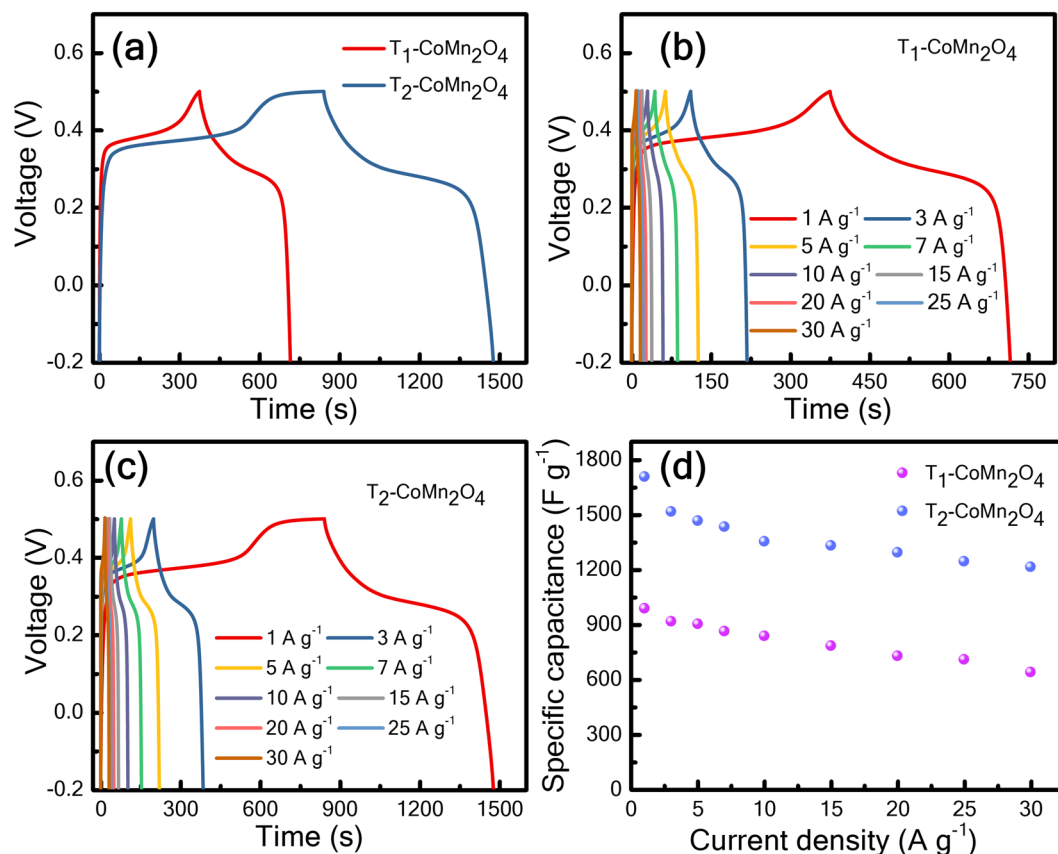
Figure 6. (**a**) Galvanostatic charge–discharge profiles of T_1-$CoMn_2O_4$ and T_2-$CoMn_2O_4$ electrodes, respectively, at a current density 1 A g^{-1}; (**b,c**) charge–discharge responses of T_1-$CoMn_2O_4$ and T_2-$CoMn_2O_4$ with current densities ranging from 1 to 30 A g^{-1}, respectively; (**c**) variation in specific capacitance with current density of T_1-$CoMn_2O_4$ and T_2-$CoMn_2O_4$.

a double-layer capacitor mechanism[14]. This phenomenon is attributed to the quasi-reversible redox reaction at the electrode–electrolyte interface[2,14]. Figure 6(a,b) show the charge–discharge profiles of T_1 and T_2 from 1 to 30 A g^{-1}, which demonstrate Faraday pseudocapacity with a negligible voltage drop.

The specific capacitance (F g^{-1}) can be calculated from the charge–discharge curve as follows[30]:

$$C_{sp} = \frac{2 \times I \times \int_{t1}^{t2} Vdt}{m \times (V_2^2 - V_1^2)} \tag{2}$$

where m, V_2, V_1, and $\int_{t_1}^{t_2} Vdt$ represent the mass of an active material, discharge current, upper voltage, lower voltage, and area covered by the discharge curve, respectively.

Moreover, C_{sp} at current densities ranging from 1 to 30 A g^{-1} is estimated using Eq. (2), and Fig. 6(d) displays the results. Figure 6(a) reveals that the discharge time of T_2 is considerably longer than that of T_1 because of the longer time for the redox reaction; therefore, C_{sp} of T_2 (1709 F g^{-1}) is considerably higher than that of T_1 (990 Fg^{-1}) at 1 A g^{-1} [Fig. 6(d)]. When the current density increased to 30 A g^{-1}, C_{sp} values of T_2 and T_1 are 1216 and 641 F g^{-1} with capacitive retention of 71% and 64%, respectively. Such high capacitive retention at high current density indicates the effect of oxygen vacancies[5]. The improved performance of T_2 is attributed to the effective sharing of oxygen vacancies causing a high degree of contact of OH$^-$ ions for Faradic reactions[31]. Note that the specific surface areas of T_1 and T_2 are nearly equal, yet, the pseudocapacitive charge storage between the two materials are distinctive; therefore, we can infer that the higher C_{sp} and retention of T_2 than those of T_1 are due to the higher oxygen vacancies concentration in T_2[32], as discussed below. In the CV procedure, the current response is measured with respect to voltage at constant time. However, galvanostatic charge–discharge (GCD) measurement is performed at a constant current for a varying voltage with respect to time. GCD measurement is generally more applicable to the study of the pesudocapacitive material[33]. A slightly higher specific capacitance is observed in this study for the GCD method compared with CV [Figs 5(d) and 6(d), respectively], which is attributed to the different measurement procedures[33].

To understand the redox nature of oxygen intercalation in $CoMn_2O_4$, ex-situ XPS of T_1 and T_2 cathode materials along with carbon black are also performed after 50 and 100 consecutive CV cycles (the results shown in the Supplementary Information, Figs S1–S3). Figure 7(a) shows different manganese oxidation states in the T_1 or T_2 cathode material evaluated after 50 and 100 CV cycles. For the cathode T_1, atomic concentrations of Mn^{3+}
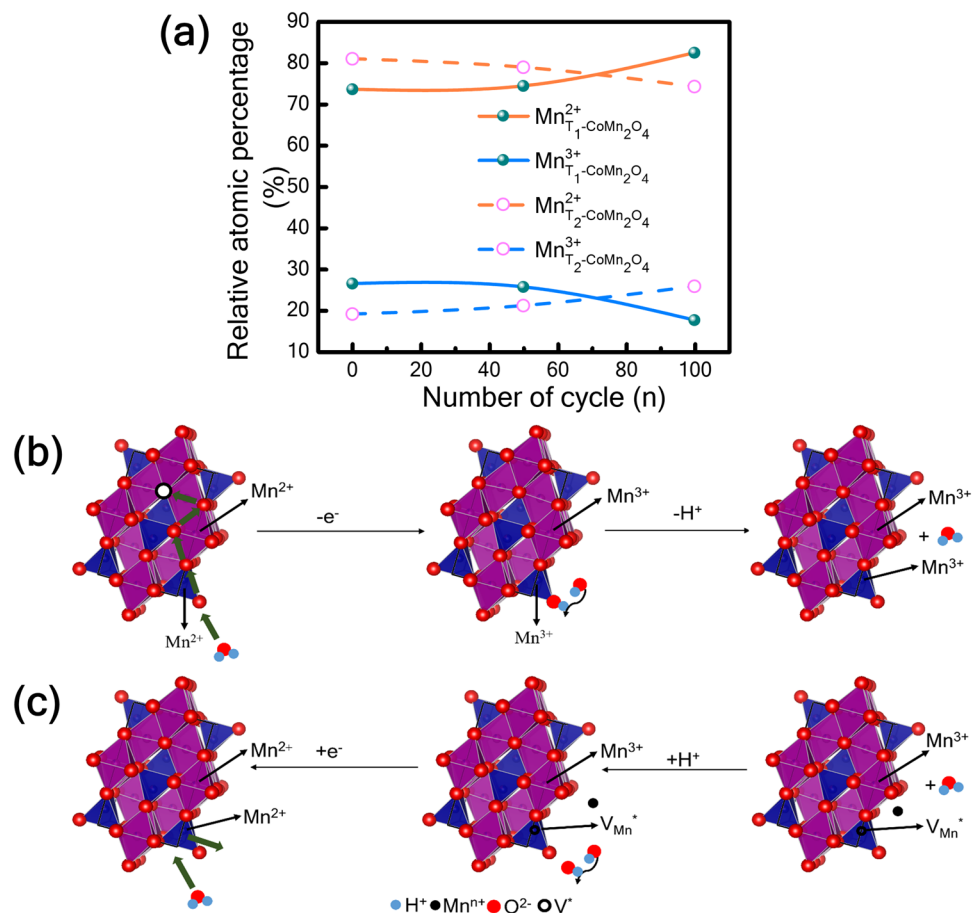
Figure 7. (**a**) Variation in manganese oxidation states in T_2 cathode after 50 and 100 cycles according to X-ray photoelectron spectroscopy and (**b,c**) mechanism of oxygen intercalation into T_2-$CoMn_2O_4$ cathode.

and Mn^{2+} remain unchanged up to 50 cycles. After 100 CV cycles, interestingly, the atomic % of Mn^{3+} and Mn^{2+} significantly change. Mn^{3+} decreases from 26 to 18 while Mn^{2+} increases from 74 to 82. As for the cathode T_2, Mn^{3+} slightly increases from 19 to 21 atomic % and Mn^{2+} decreases from 81 to 79 atomic % when changing to 50 cycles. After 100 cycles, Mn^{3+} reaches an atomic % of 26 and Mn^{2+} has 74. Therefore, the net 8% decrease of Mn^{3+} for T_1 while 7% increase for T_2 after 100 CV cycles are found. In the meantime, it is shown in Fig. 7(a) 8% increase of Mn^{2+} for T_1 and 7% decrease for T_2 after 100 cycles. On the other hand, under consideration of oxygen in the present cathode material, the O^{2-} ions from the electrolyte should have sufficient resistance to being inserted into a densely packed structure of the cathode material at room temperature to fill the oxygen vacancies without external field[32]. In addition, OH^{-1} ion from the electrolyte(0.5 M LiOH aqueous solution) would be absorbed by oxygen vacancy site leading to transfer its proton to a neighbouring lattice oxide after applied voltage. As a result, oxygen vacancy would be filled after 50 CV cycles. In general, the valence change of transition metal oxide(such as Mn), (Fig. 7(a)) is correlated with the concentration of charged oxygen vacancy, where atomic concentration of Mn^{3+} continuously increases while that of Mn^{2+} decreases up to 100 cycles in T_2 cathode material. In the mean time, the valance change in Co of T_2 cathode is not obvious(Supplemental Fig. S3(c)). In this case, the concentration of charged oxygen vacancy would be decreased. But based on Supplemental Fig. S2(c)), the concentration of oxygen vacancy gradually increases up to 100 cycles for both T_1 and T_2 cathode materials. Therefore, it seems contradiction in this case. This phenomenon may probably be attributed to the valence change of charged oxygen vacancy, complex reactions between electrolyte and composite electrode, and/or that the O1s peak contains some additional low intensity peak related to carbon material (example C=O, C-O, etc.) in the cathode affected the vacancy calculation. It needs to be proved in the future work. Figure 7(b,c) show the mechanism for the T_2 cathode material. Both T_1 and T_2 comprise multivalence Mn in lattice sites, primarily Mn^{2+} and Mn^{3+} [Fig. 4(b,c)], suggesting the electron transition occurred from $Mn^{2+} \rightarrow Mn^{3+}$ and vice versa. Through intercalation, oxygen vacancies in T_1 and T_2 cathode material are combined with oxygen, thereby altering the oxidation states of manganese. Oxygen ions are diffused, resulting in the oxidation state of Mn^{2+} to Mn^{3+}, which is validated in Fig. 7(a). Therefore, it is concluded that material T_2 has almost equal surface area and more oxygen vacancies than T_1; however, T_2 has higher capacitance, Its charge storage is believed to be due to oxygen intercalation[32]. The cobalt oxidation states of T_1 and T_2 cathode materials are almost stable after various CV cycles. This indicates that the manganese is crucial for charge storage (Supplemental Information S3).
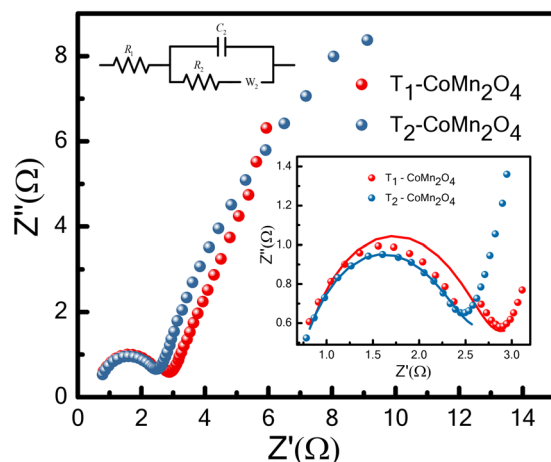
Figure 8. Electrochemical impedance spectroscopy impedance characteristics of T_1-$CoMn_2O_4$ and T_2-$CoMn_2O_4$; inset presents the high-frequency region with an equivalent circuit of T_1-$CoMn_2O_4$ and T_2-$CoMn_2O_4$.

Because of the prevalence of the electron transport and kinetic features of ions at the electrode–electrolyte interface, the pseudocapacitor exhibited a low internal resistance[14,34]. To understand this phenomenon, EIS measurements are performed at frequencies ranging from 1 Hz to 1 MHz. Figure 8 displays the conventional impedance spectra of T_1 and T_2 electrodes. The impedance behaviour introduces a semicircle in the high-frequency region and an inclined line in the low-frequency region, thus revealing pseudocapacitor behaviour[34,35]. The intercept along Z' represents the internal resistance of electrode R_1. The diameter of the semicircle provides charge transfer resistance R_2. All resistances (i.e., R_1 and R_2) of T_1 are slightly higher than those of T_2. The oxygen vacancies facilitate the migration of electrolyte ions in the conducting path[11,31,36]. Moreover, the electron conductivity of the electrode increases with the increasing number of oxygen vacancies[11,37]. Because the concentration of oxygen vacancies is higher in T_2 than in T_1, the R_1 and R_2 values of T_2 are 0.62 and 2.57 Ω, whereas those of T_1 are higher, 0.65 and 2.87 Ω, respectively. The Density Functional Theory method is applied to study the effect of oxygen vacancies on the catalytic performance of manganese oxide. Oxygen vacancies increase the conductivity because of compression of the band gap[36]. The R values of T_2 are lower than those of T_1 and are consistent with those in this study[36].

Asymmetric pseudocapacitors, including T_1//AC and T_2//AC, are fabricated, where T_1 and T_2 are the cathode and commercial AC is anode material. Figure 9(a) and (b) present the conventional CV curves of T_1 and T_2 cells at various scan rates in the voltage ranges of 0–1.6 V, which display a nearly rectangular shape. According to the CV characteristics of the T_1 cell [Fig. 9(a)], no redox peak is observed in a wide voltage window, whereas redox peaks are observed in the T_2 cells at approximately 1.5 and 1.0 V [Fig. 9(b)], indicating that T_2 cell exhibits two different energy storage mechanisms because of rapid electrolyte ion transport and redox reaction kinetics. Figure 9(c,d) represent the charge–discharge behaviours of T_1 and T_2 cells, respectively, at a current density of 1–10 A g⁻¹. T_1 cell shows an approximately linear charge–discharge behaviour, whereas T_2 cell exhibits nonlinear behaviour, indicating pseudocapacitive characteristics.

Energy density E (Wh-kg⁻¹) and power density P (W-kg⁻¹) values are calculated using Eqs (3) and (4)[18]:

$$E = \frac{1}{(2 \times 3.6)} C_{sp} \times (\Delta V)^2 \tag{3}$$

$$P = \frac{E}{\Delta t} \times 3600 \tag{4}$$

where C_{sp}, ΔV, and Δt are specific capacitance (F g⁻¹), potential window, and discharge time (s), respectively.

Figure 9(e) depicts the Ragone plots of the as-fabricated T_1 and T_2 cells, respectively. The energy density of T_2 cell decreases from 32 to 9 Wh-kg⁻¹ with an increase in power density from 0.9 to 8.7 kW-kg⁻¹, whereas for T_1 cell, the energy density decreases from 5 to 0.8 Wh-kg⁻¹ when increasing power density from 0.7 to 5 kW-kg⁻¹. T_2 exhibits higher energy density and power density than T_1. For achieving high-performance pseudocapacitors, obtaining high energy density and power density are crucial. The flake-like morphological structure [Fig. 2(b)] can improve diffusion paths for electrons and ions in the oxide materials and increase interfacial redox reactions, resulting in the increase in capacitance. Therefore, the T_2//AC device exhibited high energy and power density [Fig. 9(e)]. It is believed that the mesoporous structure and flake-like morphology increase the specific capacitance, thus increasing the energy and power density of the asymmetric pseudocapacitor, T_2. Figure 9(f) presents the cyclic stabilities of T_1 and T_2 cells, which indicate that the T_1//AC exhibits the negligible decay of capacitance (95%), whereas the T_2//AC shows 110% retention after 1000 cycles in the PVA-LiOH polymer gel electrolyte at 2 A g⁻¹. This observation indicates the excellent electrochemical stability of T_1 and T_2 cells. The slight decay of
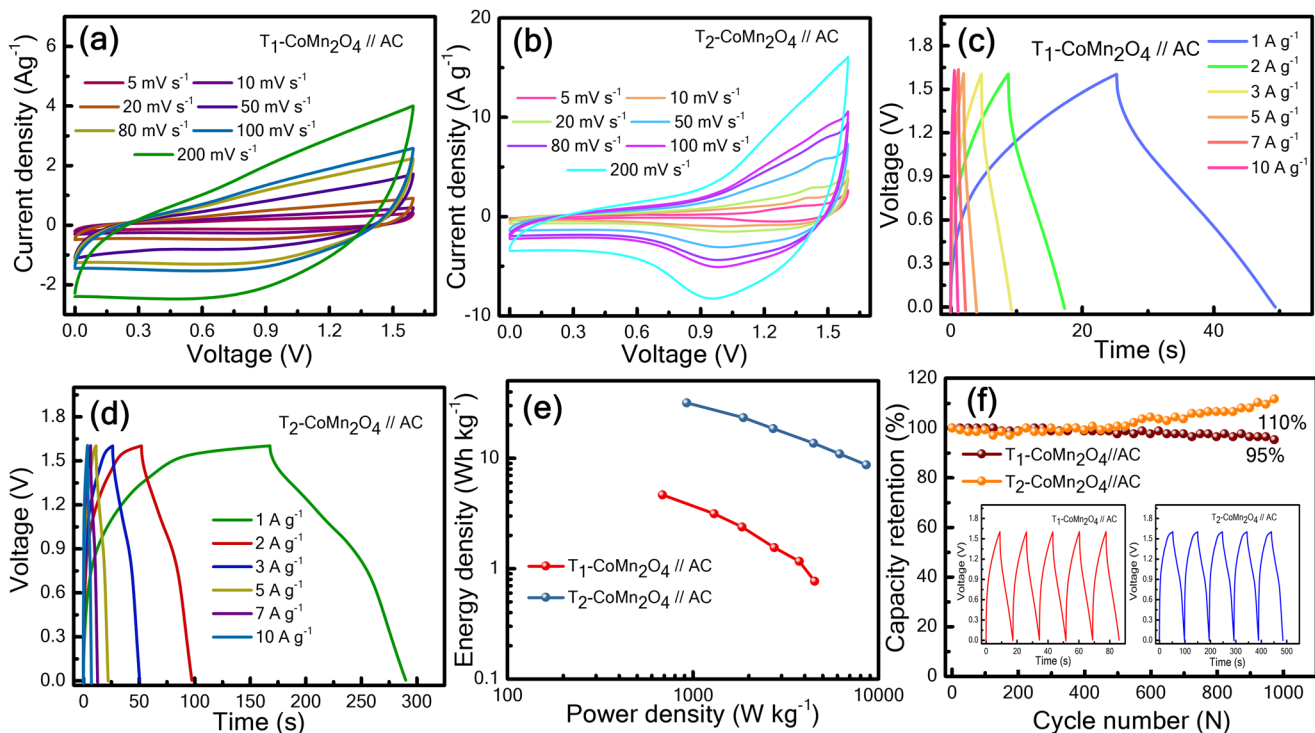
Figure 9. Electrochemical performance of the asymmetric psudocapacitor device: (**a,b**) cyclic voltammetry responses of the asymmetric device containing T_1-CoMn$_2$O$_4$//AC and T_2-CoMn$_2$O$_4$//AC, respectively, at scan rates ranging from 5–200 mV s^{-1}; (**c,d**) galvanostatic charge–discharge profiles of T_1-CoMn$_2$O$_4$//AC and T_2-CoMn$_2$O$_4$//AC, respectively, with current densities from 1–10 A g^{-1}; (**e**) Ragone plots of power density versus energy density for T_1-CoMn$_2$O$_4$//AC and T_2-CoMn$_2$O$_4$//AC asymmetric pseudocapacitor devices; (**f**) cycle performance of T_1-CoMn$_2$O$_4$//AC and T_2-CoMn$_2$O$_4$//AC asymmetric pseudocapacitors with a discharge current density of 2 A g^{-1}. The inset presents the galvanostatic charge–discharge curve of the asymmetric pseudocapacitor device.

cyclic stability for T_1//AC is possibly attributed to the decrease in the adhesion of active materials with the current collector[27]. These results reveal that cobalt manganese oxide is a prominent electrode candidate material for making asymmetric pseudocapacitors.

Conclusions

Modulation of the intrinsic defect concentration in CoMn$_2$O$_4$ tetragonal spinel was synthesised at moderate temperatures by adjusting the mixing sequence of Co and Mn precursors. Moreover, two distinct morphologies of CoMn$_2$O$_4$ were observed as a result of this adjustment. CoMn$_2$O$_4$ synthesised by mixing the Mn precursor after adding the Co precursor (T_1) formed nanoparticle morphology. Moreover, a nanoparticle and nanoflake combined structure was formed when the Mn precursor was mixed before adding the Co precursor (T_2). The electrochemical evaluations revealed that the T_2 electrode had a higher specific capacitance (1709 F g^{-1}) than the T_1 electrode (990 F g^{-1}) at 1 A g^{-1} with capacitive retentions of 71% and 64% for T_2 and T_1, respectively. A higher number of oxygen vacancies existed in the T_2 electrode, which enhanced the capacitance because of the intercalation of oxygen ions/oxygen vacancies from the aqueous alkaline electrolyte. The T_2//AC asymmetric pseudocapacitor exhibited a maximum energy density of 32 Wh-kg^{-1} at a power density of 0.9 kW-kg^{-1}. The T_2//AC pseudocapacitor had a higher energy density and power density than T_1//AC. Both T_1 and T_2 cells demonstrated excellent electrochemical stability. This study not only demonstrates that the mixing sequence of the precursors during CoMn$_2$O$_4$ synthesis is crucial in determining the performance of the pseudocapacitor but also provides insights into the mechanism of charge storage with oxygen vacancies. The present study develops a new type of CoMn$_2$O$_4$-based electrode for future pseudocapacitor applications.

Methods

Materials.   To synthesise the nanocrystalline cobalt manganese oxide spinel materials, the precursor materials of cobalt nitrate hexahydrate [Co (NO$_3$)$_2$, 6H$_2$O] (Alfa Aesar), manganese nitrate tetrahydrate [Mn(NO$_3$)$_2$, 4H$_2$O] (Alfa Aesar), and an aqueous ammonia solution were used. All chemicals were used without any purification.

Synthesis of the CoMn$_2$O$_4$ spinel structure.   In accordance with a conventional process, 25 ml of 0.2 M [Co(NO$_3$)$_2$, 6H$_2$O] was stirred at room temperature, and 20 ml of ammonia solution was slowly added to this solution. Moreover, 50 ml of 0.2 M [Mn(NO$_3$)$_2$, 4H$_2$O] was subsequently added dropwise to the mixture and stirred for 2 h. To decompose nitrates, the mixture was vacuum-filtered and heated at 180 °C for 1 h in the air, and

the sample was denoted as T_1-CoMn$_2$O$_4$ (T_1). Similarly, another sample was synthesised using the same stoichiometric amounts of Co and Mn precursors as the first sample; however, 25 ml of 0.2 M [Co(NO$_3$)$_2$, 6H$_2$O] was added after adding [Mn(NO$_3$)$_2$, 4H$_2$O]. The sample was denoted as T_2-CoMn$_2$O$_4$ (T_2).

Material characterisation. To identify the crystal structure powder, XRD was conducted with Cu Kα radiation using a Bruker D2 PHASER. The specific surface area of nanomaterials was characterised by the BET surface area analyser (ASAP, 2020). SEM was conducted to study the surface microstructure (Hitachi SU-8010). A high-resolution TEM analysis was used to analyse the formation of the nanostructure and composition of materials (JEOL JEM-2010F). To examine the oxidation states of spinel oxides, XPS (ULVAC-PHI Quantera SXM) was performed.

Preparation of working electrodes. To fabricate the working electrode, active material powders were mixed in the N-methyl-2-pyrrolidone (NMP) solution to form a uniform slurry of 10 mg/ml. A porous nickel foam substrate was washed with acetone and etched using a 6 M HCl solution for 30 min. After being washed using deionised water (DI water), the substrate was dried at 70 °C for 6 h. Next, the slurry containing active materials was coated onto the substrate (area of 1 cm^2) using a brush and dried at 80 °C for 15 h under a vacuum condition to study its electrochemical properties and mechanisms. The mass loadings of T_1 and T_2 were 0.3 and 0.15 mg, respectively.

Asymmetric pseudocapacitor assembly. The asymmetric pseudocapacitor was fabricated using activated carbon (AC) as an anode material, and T_1 or T_2 was used as a cathode material. The anode electrode was prepared using a mixture of AC, a polyvinylidene fluoride (PVDF) binder, and carbon black in a weight ratio of 85:10:5 in a N-methylpyrrolidone (NMP) solution to form homogeneous dispersion for deposition on the substrate. For fabricating a cathode electrode, active materials (T_1 or T_2), PVDF, and carbon black were used in a weight ratio of 75:10:15 and dispersed in the NMP solution. The slurries (T_1 and T_2) were coated on the nickel foam substrates (current collector) and dried at 80 °C for 15 h in a vacuum to form the cathodes.

To assemble pseudocapacitor devices, the solid-state electrolyte was first prepared: 1 g of PVA and 1 g of LiOH were dispersed in 20 ml of water and heated at 90 °C to form a transparent gel. After cooling, cathode and anode electrodes were then immersed on the gel electrolyte and dried at room temperature. Both electrodes were pressed to fabricate hybrid supercapacitors and were denoted as T_1-CoMn$_2$O$_4$/PVA-LiOH/AC (T_1 cell) and T_2-CoMn$_2$O$_4$/PVA-LiOH/AC (T_2 cell). For an asymmetric pseudocapacitor, the charges (Q) for cathode and anode electrodes were balanced using the following equation: $Q = Cm\Delta E$, where C, m, and ΔE are the specific capacitance, mass of active materials, and potential window, respectively. After calculations, the total masses of T_1 and T_2 cell devices were approximately 1.5 and 0.5 mg, respectively.

Electrochemical characterisation. The electrochemical performances of electrodes and pseudocapacitors were measured using an electrochemical analyser (Instruments CHI618B), which included CV, galvanostatic charge–discharge cycling (GCC), and EIS. Electrochemical characterisations of the electrode materials were performed using three-electrode cells with a saturated calomel electrode, platinum as a counter electrode, a working electrode of an active material deposited on the Ni foam, and 0.5 M LiOH serving as the electrolyte. The working electrode was immersed in the electrolyte for providing suitable contact between the electrode and electrolyte.

Data availability
Readers can access data by contacting the corresponding author.

References
1. Liu, M. *et al.* One-step synthesis of graphene nanoribbon–MnO$_2$ hybrids and their all-solid-state asymmetric supercapacitors. *Nanoscale* **6**, 4233 (2014).
2. Conway, B. E., Birss, V. & Wojtowicz, J. The role and utilization of pseudocapacitance for energy storage by supercapacitors. *J. Power Sources* **66**, 1–14 (1997).
3. Sankar, K. V., Selvan, R. K. & Meyrick, D. Electrochemical performances of CoFe$_2$O$_4$ nanoparticles and a rGO based asymmetric supercapacitor. *RSC Adv.* **5**, 99959–99967 (2015).
4. Bijelić, M. *et al.* Long cycle life of CoMn$_2$O$_4$ lithium ion battery anodes with high crystallinity. *J. Mater. Chem. A* **3**, 14759–14767 (2015).
5. Gao, R. *et al.* The role of oxygen vacancies in improving the performance of CoO as a bifunctional cathode catalyst for rechargeable Li–O$_2$. *batteries. J. Mater. Chem. A* **3**, 17598–17605 (2015).
6. Lavela, P., Tirado, J. L. & Vidal-Abarca, C. Sol–gel preparation of cobalt manganese mixed oxides for their use as electrode materials in lithium cells. *Electrochim. Acta* **52**, 7986–7995 (2007).
7. Liang, Y. *et al.* Covalent Hybrid of Spinel Manganese–Cobalt Oxide and Graphene as Advanced Oxygen Reduction Electrocatalysts. *J. Am. Chem. Soc.* **134**, 3517–3523 (2012).
8. Zhou, L., Zhao, D. & Lou, X. W. Double-Shelled CoMn$_2$O$_4$ Hollow Microcubes as High-Capacity Anodes for Lithium-Ion Batteries. *Adv. Mater.* **24**, 745–748 (2012).
9. Lu, J. *et al.* Effectively suppressing dissolution of manganese from spinel lithium manganate via a nanoscale surface-doping approach. *Nat. Commun.* **5**, 5693 (2014).
10. Menezes, P. W., Indra, A., Gutkin, V. & Driess, M. Boosting electrochemical water oxidation through replacement of O h Co sites in cobalt oxide spinel with manganese. *Chem. Commun.* **53**, 8018–8021 (2017).

10

11. Sadighi, Z. *et al*. Positive role of oxygen vacancy in electrochemical performance of $CoMn_2O_4$ cathodes for $Li-O_2$ batteries. *J. Power Sources* **365**, 134–147 (2017).
12. Ding, L., Yang, W., Chen, L., Cheng, H. & Qi, Z. Fabrication of spinel $CoMn_2O_4$ hollow spheres for highly selective aerobic oxidation of 5-hydroxymethylfurfural to 2,5-diformylfuran. *Catal. Today* 0–1, https://doi.org/10.1016/j.cattod.2018.04.069 (2018).
13. Guo, W. *et al*. Spinel $CoMn_2O_4$ nanoparticles supported on a nitrogen and phosphorus dual doped graphene aerogel as efficient electrocatalysts for the oxygen reduction reaction. *RSC Adv*. **6**, 96436–96444 (2016).
14. Meher, S. K. & Rao, G. R. Effect of Microwave on the Nanowire Morphology, Optical, Magnetic, and Pseudocapacitance Behavior of Co_3O_4. *J. Phys. Chem. C* **115**, 25543–25556 (2011).
15. Ding, R., Qi, L. & Wang, H. A facile and cost-effective synthesis of mesoporous $NiCo_2O_4$ nanoparticles and their capacitive behavior in electrochemical capacitors. *J. Solid State Electrochem*. **16**, 3621–3633 (2012).
16. Dubal, D. P., Jagadale, A. D. & Lokhande, C. D. Big as well as light weight portable, Mn_3O_4 based symmetric supercapacitive devices: Fabrication, performance evaluation and demonstration. *Electrochim. Acta* **80**, 160–170 (2012).
17. Li, J., Xiong, S., Li, X. & Qian, Y. A facile route to synthesize multiporous $MnCo_2O_4$ and $CoMn_2O_4$ spinel quasi-hollow spheres with improved lithium storage properties. *Nanoscale* **5**, 2045 (2013).
18. Kumar, N. *et al*. Probing the electrochemical properties of an electrophoretically deposited Co_3O_4/rGO/CNTs nanocomposite for supercapacitor applications. *RSC Adv*. **6**, 60578–60586 (2016).
19. Thota, S. *et al*. Neutron diffraction study of the inverse spinels Co_2TiO_4 and Co_2SnO_4. *Phys. Rev. B* **96**, 144104 (2017).
20. Si, C. *et al*. Nanoporous Platinum/$(Mn,Al)_3O_4$ Nanosheet Nanocomposites with Synergistically Enhanced Ultrahigh Oxygen Reduction Activity and Excellent Methanol Tolerance. *ACS Appl. Mater. Interfaces* **9**, 2485–2494 (2017).
21. Galakhov, V. R. *et al*. Mn 3s exchange splitting in mixed-valence manganites. *Phys. Rev. B* **65**, 113102 (2002).
22. Beyreuther, E., Grafström, S., Eng, L. M., Thiele, C. & Dörr, K. XPS investigation of Mn valence in lanthanum manganite thin films under variation of oxygen content. *Phys. Rev. B* **73**, 155425 (2006).
23. Toupin, M., Brousse, T. & Bélanger, D. Charge Storage Mechanism of MnO_2 Electrode Used in Aqueous Electrochemical Capacitor. *Chem. Mater*. **16**, 3184–3190 (2004).
24. Bharti, B., Kumar, S., Lee, H.-N. & Kumar, R. Formation of oxygen vacancies and Ti^{3+} state in TiO_2 thin film and enhanced optical properties by air plasma treatment. *Sci. Rep*. **6**, 32355 (2016).
25. Jing, M. *et al*. Electrochemically alternating voltage tuned Co_2MnO_4/Co hydroxide chloride for an asymmetric supercapacitor. *Electrochim. Acta* **165**, 198–205 (2015).
26. Halder, L. *et al*. High performance advanced asymmetric supercapacitor based on ultrathin and mesoporous $MnCo_2O_{4.5}$-$NiCo_2O_4$ hybrid and iron oxide decorated reduced graphene oxide electrode materials. *Electrochim. Acta* **283**, 438–447 (2018).
27. Yan, J. *et al*. Advanced Asymmetric Supercapacitors Based on $Ni(OH)_2$/Graphene and Porous Graphene Electrodes with High Energy Density. *Adv. Funct. Mater*. **22**, 2632–2641 (2012).
28. Rahmanifar, M. S. *et al*. A dual Ni/Co-MOF-reduced graphene oxide nanocomposite as a high performance supercapacitor electrode material. *Electrochim. Acta* **275**, 76–86 (2018).
29. Su, Z. *et al*. Co-electro-deposition of the MnO_2–PEDOT:PSS nanostructured composite for high areal mass, flexible asymmetric supercapacitor devices. *J. Mater. Chem. A* **1**, 12432 (2013).
30. Roldán, S. *et al*. An approach to classification and capacitance expressions in electrochemical capacitors technology. *Phys. Chem. Chem. Phys*. **17**, 1084–1092 (2015).
31. Lee, J.-H. *et al*. The role of vacancies and defects in $Na_{0.44}MnO_2$ nanowire catalysts for lithium–oxygen batteries. *Energy Environ. Sci*. **5**, 9558 (2012).
32. Mefford, J. T., Hardin, W. G., Dai, S., Johnston, K. P. & Stevenson, K. J. Anion charge storage through oxygen intercalation in $LaMnO_3$ perovskite pseudocapacitor electrodes. *Nat. Mater*. **13**, 726–732 (2014).
33. Feng, X. *et al*. The self-assembly of shape controlled functionalized graphene–MnO_2 composites for application as supercapacitors. *J. Mater. Chem. A* **2**, 9178–9184 (2014).
34. Pawar, S. M. *et al*. Multi-functional reactively-sputtered copper oxide electrodes for supercapacitor and electro-catalyst in direct methanol fuel cell applications. *Sci. Rep*. **6**, 21310 (2016).
35. Inamdar, A. I. *et al*. Chemically grown, porous, nickel oxide thin-film for electrochemical supercapacitors. *J. Power Sources* **196**, 2393–2397 (2011).
36. Li, L. *et al*. Insight into the Effect of Oxygen Vacancy Concentration on the Catalytic Performance of MnO_2. *ACS Catal*. **5**, 4825–4832 (2015).
37. Recham, N. *et al*. A 3.6 V lithium-based fluorosulphate insertion positive electrode for lithium-ion batteries. *Nat. Mater*. **9**, 68–74 (2010).

Acknowledgements

Author contributions

T.Y.T. and K.H.W. conceived the idea and supervised the work. B.P. performed all of the experimental and characterisation processes with the help of F.M.S. and A.K. and P.A.L. assisted in some material characterisations. B.P., F.M.S., D.P. and C.C.Y. analysed the data. B.P. wrote the manuscript. T.Y.T. corrected and finalised the manuscript. All authors reviewed the final manuscript.

Competing interests

The authors declare no competing interests.

Additional information

Supplementary information is available for this paper at https://doi.org/10.1038/s41598-019-53364-2.

Correspondence and requests for materials should be addressed to T.–.T.

Reprints and permissions information is available at www.nature.com/reprints.

Publisher's note Springer Nature remains neutral with regard to jurisdictional claims in published maps and institutional affiliations.